

Structure of voltage-dependent anion channel-tethered bilayer lipid membranes determined using neutron reflectivity

David P. Hoogerheide,^{a*} Sergei Yu. Noskov,^b Adam J. Kuszak,^{c‡} Susan K. Buchanan,^c Tatiana K. Rostovtseva^d and Hirsh Nanda^{a,e§}

Received 26 February 2018
Accepted 20 August 2018

Edited by V. T. Forsyth, Institut Laue-Langevin, France, and Keele University, UK

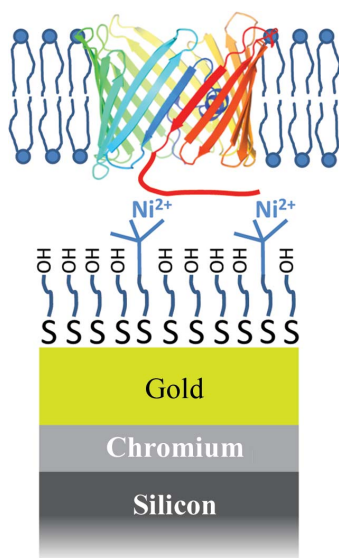
‡ Current affiliation: Office of Dietary Supplements, Office of the Director, National Institutes of Health, Bethesda, Maryland, USA.
§ Current affiliation: Johnson & Johnson, Spring House, Pennsylvania, USA.

Keywords: neutron reflectivity; protein-tethered bilayer lipid membranes; protein reconstitution; voltage-dependent anion channel.

Supporting information: this article has supporting information at journals.iucr.org/d

^aCenter for Neutron Research, National Institute of Standards and Technology, Gaithersburg, MD 20878, USA, ^bCentre for Molecular Simulations and Department of Biological Sciences, University of Calgary, Calgary T2N 1N4, Canada, ^cLaboratory of Molecular Biology, National Institute of Diabetes and Digestive and Kidney Diseases, National Institutes of Health, Bethesda, MD 20892, USA, ^dSection on Molecular Transport, Eunice Kennedy Shriver National Institute of Child Health and Human Development, National Institutes of Health, Bethesda, MD 20892, USA, and ^ePhysics Department, Carnegie Mellon University, Pittsburgh, PA 15213, USA. *Correspondence e-mail: david.hoogerheide@nist.gov

Neutron reflectivity (NR) has emerged as a powerful technique to study the structure and behavior of membrane proteins at planar lipid interfaces. Integral membrane proteins (IMPs) remain a significant challenge for NR owing to the difficulty of forming complete bilayers with sufficient protein density for scattering techniques. One strategy to achieve high protein density on a solid substrate is the capture of detergent-stabilized, affinity-tagged IMPs on a nitrilotriacetic acid (NTA)-functionalized self-assembled monolayer (SAM), followed by reconstitution into the lipids of interest. Such protein-tethered bilayer lipid membranes (ptBLMs) have the notable advantage of a uniform IMP orientation on the substrate. Here, NR is used to provide a structural characterization of the ptBLM process from formation of the SAM to capture of the detergent-stabilized IMP and lipid reconstitution. The mitochondrial outer-membrane voltage-dependent anion channel (VDAC), which controls the exchange of bioenergetic metabolites between mitochondria and the cytosol, was used as a model β -barrel IMP. Molecular dynamics simulations were used for comparison with the experimental results and to inform the parameters of the physical models describing the NR data. The detailed structure of the SAM is shown to depend on the density of the NTA chelating groups. The relative content of detergent and protein in surface-immobilized, detergent-stabilized VDAC is measured, while the reconstituted lipid bilayer is shown to be complete to within a few percent, using the known atomic structure of VDAC. Finally, excess lipid above the reconstituted bilayer, which is of consequence for more indirect structural and functional studies, is shown to be present.



1. Introduction

Membrane proteins play critical roles in normal cellular function, pathologies and treatment. While integral membrane proteins are estimated to constitute only about 20% of the human proteome (Almén *et al.*, 2009), they represent about 70% of modern drug targets (Yildirim *et al.*, 2007). This disproportionate importance is owing to three fundamental characteristics. Firstly, because the membranes in which these proteins are embedded serve as barriers between cellular compartments and between the interior and exterior of the cell, many integral membrane proteins are either gatekeepers of ion and metabolite fluxes across the membrane or transducers of molecular signaling cascades. Secondly, the lipid environment of membrane proteins provides a sensitive means by which cells regulate their activity (Yeagle, 2014).

Thirdly, the localization of membrane proteins to the two-dimensional membrane surface provides an increase in the effective concentration of membrane-binding drugs, and hence in the rates of their reaction (Mosior & McLaughlin, 1992; Berg & von Hippel, 1985). Besides, owing to their strategic location, relatively few copies of integral membrane proteins are required for effective cellular function.

From a technical perspective, however, these very characteristics of integral membrane proteins – their relative scarcity and their sensitivity to the lipid environment – make them particularly difficult to study using traditional solution-based biophysical and biochemical techniques. As a result, significant and diverse efforts have been expended to develop strategies to immobilize membrane proteins in a manner suitable for structural and/or functional study and for use as biosensors. These techniques have employed a variety of approaches for associating bilayer membranes with surfaces (Wetzer *et al.*, 1997; Majewski *et al.*, 1998; Wagner & Tamm, 2000; Fragneto *et al.*, 2001; Castellana & Cremer, 2006; McGillivray *et al.*, 2007; Früh *et al.*, 2011; Jackman *et al.*, 2012; Robertson *et al.*, 2012) and various methods for the subsequent or concomitant incorporation of membrane proteins (McGillivray *et al.*, 2009; Bertram *et al.*, 2015; Soranzo *et al.*, 2017; Maccarini *et al.*, 2017; Veneziano *et al.*, 2017).

One such strategy involves leveraging the well developed affinity-tag purification techniques to specifically capture detergent-stabilized membrane proteins onto a surface and then reconstruct a bilayer of the desired composition around the membrane protein (Giess *et al.*, 2004). This technique forms so-called ‘protein-tethered bilayer lipid membranes’ (ptBLMs), which are distinct from traditional tethered bilayer lipid membranes (tBLMs) in that the tethering is accomplished through the target protein, thereby ensuring that extramembrane domains of the protein on the surface-proximal side of the bilayer have sufficient space to fold and function naturally. The particular advantage of ptBLMs is that the proteins are attached to the surface in a uniform orientation. Furthermore, if the ptBLM can be made complete (*i.e.* covering the entire surface without large defects), it can be used to study electrical and physical transport. The chemical structure and lateral structure of ptBLMs have been extensively studied by surface-enhanced infrared spectroscopy (Ataka *et al.*, 2004) and atomic force microscopy (Bronder *et al.*, 2016; Sumino *et al.*, 2017). Previous neutron reflectivity studies of ptBLMs of the leucine transporter demonstrated successful but incomplete ptBLM formation (Jagalski *et al.*, 2015).

In this work, we employ neutron reflectivity (NR) to probe the structural details of a complete protein-tethered bilayer lipid membrane. NR is a nonperturbative scattering technique that can distinguish between protein and lipid components in the ptBLM. NR is also exquisitely sensitive to the water content of a bilayer, and thus is especially useful for studying bilayer completeness. The membrane protein that we chose to form ptBLMs is the most abundant protein of the mitochondrial outer membrane: the voltage-dependent anion channel (VDAC1). Since its successful crystallization and structural

determination (Ujwal *et al.*, 2008; Hiller *et al.*, 2008; Bayrhuber *et al.*, 2008), VDAC has been the subject of several functional studies involving tBLM formation from proteoliposomes (Veneziano *et al.*, 2017; Kozuch *et al.*, 2014) and structural studies using nanodisc encapsulation and NMR (Nasr *et al.*, 2017).

VDAC plays a crucial role in the regulation of ATP production, Ca²⁺ homeostasis, apoptosis and steroidogenesis (Shoshan-Barmatz *et al.*, 2010; Maldonado & Lemasters, 2014; Rostovtseva & Bezrukov, 2008; Rostovtseva *et al.*, 2005; Reina & De Pinto, 2017; Shoshan-Barmatz *et al.*, 2017), thus proving to be indispensable for proper mitochondrial function and consequently for normal cell physiology. This large β -barrel passive transport channel serves as a unique pathway across the outer membrane for all water-soluble mitochondrial respiratory substrates such as ATP, ADP and small ions (Colombini, 2004). VDAC regulates these fluxes between mitochondria and the cytosol using its conserved ability to ‘gate’ or adopt different conducting and selectivity states (Hodge & Colombini, 1997; Lemasters *et al.*, 2012; Rostovtseva & Bezrukov, 2008). Transitions from open to closed involve large conformational rearrangements of the channel, leading to a decrease in pore dimensions and channel volume and alteration of ion selectivity (Colombini, 2004; Zimmerberg & Parsegian, 1986; Song *et al.*, 1998; Colombini *et al.*, 1996), resulting in a decreased permeability for negatively charged metabolites. Therefore, VDAC gating affects delivery of ATP to the cytosol as well as access of ADP to the electron-transport chain complexes in the mitochondrial inner membrane, thus directly modulating mitochondrial oxidative phosphorylation. Although the available VDAC structures represent the open state, while the structure(s) of closed states remain to be determined, resolving how the channel transitions between states is crucial for our understanding of the mechanism(s) of mitochondrial control and modulation of oxidative phosphorylation.

It has recently become clear that VDAC also accomplishes regulation of metabolite flux through interaction with cytosolic regulatory partners (Rostovtseva *et al.*, 2017), including tubulin heterodimers (Rostovtseva *et al.*, 2008) and Parkinson disease-related α -synuclein (Rostovtseva *et al.*, 2015). The structures of membrane-bound α -synuclein (Braun *et al.*, 2014; Fusco *et al.*, 2014; Jiang *et al.*, 2017) and tubulin (Hoogerheide *et al.*, 2017) have been determined, but the structures of the complexes between VDAC and either tubulin or α -synuclein have not yet been determined. We believe that ptBLMs are a promising platform for studies of these and other integral/peripheral membrane-protein complexes.

Here, we use NR to demonstrate that complete ptBLMs can be formed from the VDAC protein. We provide a step-by-step structural characterization of VDAC in a lipid-reconstituted environment, beginning with measurements of the self-assembled monolayer (SAM) used to present nickel-chelated nitrilotriacetic acid (NTA) groups to the measurement surface. The properties of detergent-stabilized, polyhistidine-tagged VDAC captured on the NTA-functionalized SAM were then determined. Finally, we demonstrate the formation of a

complete lipid bilayer incorporating VDAC at a high density, characterize its robustness against acidification and discuss some of the challenges in protein reconstitution and functional characterization. Molecular dynamics (MD) simulations are used to inform the parameters of the structural models, while the excellent agreement between the lipid structures determined by equilibrium MD simulations and by NR serves to validate this approach.

2. Materials and methods

2.1. Buffers

Unless stated otherwise, all experiments were performed in an aqueous solution of 50 mM ($M = \text{mol dm}^{-3}$) tris(hydroxymethyl)aminomethane (Tris) buffered at pH 8, 150 mM sodium chloride, 0.5 mM tris(2-carboxyethyl)phosphine (TCEP) and 0.075% *n*-dodecyl-*N,N*-dimethylamine-*N*-oxide or lauryldimethylamine oxide (LDAO) detergent (Anatrace).

2.2. Expression and purification of mVDAC1-GSG-His₆

2.2.1. Expression of mVDAC1-GSG-His₆. The full-length amino-acid sequence of the *Mus musculus* VDAC1 protein (NCBI Reference Sequence NP_035824.1) was codon-optimized for bacterial expression and synthetically created in a pUC57 plasmid (GenScript; the nucleotide sequences are available upon request). The *M. musculus* VDAC1 coding sequence was then inserted into an isopropyl β -D-1-thiogalactopyranoside-inducible pET-28 vector (Novagen/EMD Millipore), with a C-terminal linker (Gly-Ser-Gly) followed by a 6 \times His purification tag, using ligation-independent cloning methods (Aslanidis & de Jong, 1990; primers are available upon request). The resulting mVDAC1-GSG-His₆ plasmid was used to transform T7 Express competent *Escherichia coli* cells (New England Biolabs), which were grown in 2 \times YT liquid medium in the presence of 30 $\mu\text{g ml}^{-1}$ kanamycin at 37°C to an A_{600} of 0.6 and then induced by the addition of 0.5 mM isopropyl β -D-1-thiogalactopyranoside and incubated for 3–4 h at 37°C. mVDAC1-GSG-His₆-expressing *E. coli* cells were harvested at 6700g, resuspended in ice-cold 20 mM Tris-HCl pH 8, 200 mM NaCl, 10 mM MgCl₂, 100 $\mu\text{g ml}^{-1}$ 4-(2-aminoethyl)benzenesulfonyl fluoride, 10 $\mu\text{g ml}^{-1}$ DNase I and lysed by three passages through an EmulsiFlex-C3 homogenizer (Avestin). VDAC1-containing inclusion bodies (IBs) were collected *via* centrifugation at 12 000g, resuspended in 50 mM Tris-HCl pH 8, 200 mM NaCl, 1 mM EDTA, 2% (*w/v*) Triton X-100 and stirred for 30 min at 20°C. The detergent was washed away and the IBs were collected by sequential centrifugation at 12 000g and resuspended in 50 mM Tris-HCl pH 8, 200 mM NaCl.

2.2.2. Refolding and purification of mVDAC1-GSG-His₆. Pelleted mVDAC1-GSG-His₆ IBs were solubilized in 20 mM Tris-HCl pH 8, 300 mM NaCl, 6 M guanidine-HCl, 1 mM TCEP at 10 mg ml⁻¹ at 20°C. After centrifugation at 10 000g, the resulting supernatant had a final protein concentration of 2–3 mg ml⁻¹. Solubilized, denatured mVDAC1-GSG-His₆

(50 ml) was then applied onto a nickel-nitrilotriacetic acid (Ni-NTA) agarose column (Qiagen; 12 ml bed volume) equilibrated in 20 mM Tris-HCl pH 8, 300 mM NaCl, 6 M guanidine-HCl. Nonspecifically bound protein was washed off using equilibration buffer plus 20 mM imidazole, and mVDAC1-GSG-His₆ was eluted with equilibration buffer plus 300 mM imidazole. Ni-NTA elution fractions containing mVDAC1-GSG-His₆ were pooled and the protein was refolded by dropwise, tenfold dilution into refolding buffer [50 mM Tris-HCl pH 8, 150 mM NaCl, 5 mM TCEP, 0.5% (*w/v*) LDAO detergent]. The refolding reaction was stirred for 1 h at 20°C and then subjected to two rounds of tenfold dialysis at 4°C against 50 mM Tris-HCl pH 8, 150 mM NaCl, 1 mM TCEP, 0.075% LDAO using 12 kDa molecular-mass cutoff dialysis tubing (Sigma-Aldrich).

After a third tenfold dialysis at 4°C against 50 mM Tris-HCl pH 8, 0.5 mM TCEP, 0.075% LDAO to reduce the NaCl concentration to 15 mM, impurities and aggregates were removed *via* Q Sepharose high-performance anion-exchange chromatography (GE Healthcare) in 50 mM Tris-HCl pH 8, 0.075% LDAO, 0.01% (*w/v*) NaN₃, 0.5 mM TCEP, 0.5 mM EDTA with a 0–40 mM NaCl gradient. The Q Sepharose column flowthrough fraction, which contained refolded mVDAC1-GSG-His₆, was applied onto a Ni-NTA agarose column (15 ml bed volume) equilibrated with 50 mM Tris-HCl pH 8, 150 mM NaCl, 0.5 mM TCEP, 0.075% LDAO. mVDAC1-GSG-His₆ was eluted using the same buffer plus 250 mM imidazole. Fractions containing VDAC1 were concentrated with 30 kDa molecular-weight cutoff Centrprep Ultracel YM filters (EMD Millipore).

Final isolation and buffer exchange of the refolded mVDAC1-GSG-His₆ sample was performed *via* size-exclusion chromatography with HiPrep 16/60 Sephacryl S-300 HR preparative columns (GE Healthcare) run at 4°C in 50 mM Tris-HCl pH 8, 150 mM NaCl, 0.075% LDAO, 0.01% NaN₃, 0.5 mM TCEP. Blue dextran, ovalbumin, bovine serum albumin and chymotrypsinogen A standard proteins (GE Healthcare) were used to calibrate the size-exclusion column. The fractionation and purity of mVDAC1-GSG-His₆ was monitored throughout by SDS-PAGE separation and Coomassie staining.

2.3. Sample-wafer preparation

Silicon wafers (100 orientation, n-doped with phosphorus to a resistivity of 1–100 $\Omega \text{ cm}$) of 5 mm thickness and 75 mm diameter were coated with about 30 Å of chromium followed by at least 100 Å of gold by RF magnetron sputtering using a Denton Vacuum Discovery 550 Sputtering System at the National Institute for Standards and Technology (NIST) Center for Nanoscale Science and Technology cleanroom. The sputtering used an argon flow rate of 11 cm³ min⁻¹, an RF power of 250 W (Cr) or 100 W (Au) and a chamber pressure of less than 1 mTorr. The gold root-mean-squared roughness was 5 Å or less after coating.

2.4. Self-assembled monolayer (SAM) formation

NTA-functionalized surfaces were created from thiolated oligo(ethylene oxide)-based compounds 1 (NTA-terminated) and 2 (hydroxy-terminated) as described previously (Vaish *et al.*, 2013). These compounds, each of which comprises six ethylene oxide repeats linking the thiol group to the terminal NTA or hydroxyl moiety, will be referred to as OEG-NTA and OEG, respectively. Aqueous solutions with a total concentration of 0.2 mM OEG and OEG-NTA were formulated at the desired molar ratios. Glacial acetic acid was added to 3% to suppress oligomerization. Gold-coated sample wafers (see Section 2.3) were soaked in these solutions immediately after coating for at least 8 h and then rinsed thoroughly with deionized water before use.

2.5. Neutron reflectometry

NR experiments were carried out on the NG7 horizontal reflectometer at the NIST Center for Neutron Research (NCNR). The SAM-coated surface of the sample wafer was mounted in a flow cell facing a 100 μm reservoir, as defined by a 65 mm inner diameter cylindrical Viton gasket separating the sample wafer from a thicker backing wafer. The backing wafer was perforated to provide a single inlet and outlet, which were coupled by flat-bottomed fittings to external tubing for solution exchanges. The resulting flow cell had a total volume of about 1.5 ml (about 0.5 ml in the measurement region). A monochromatic beam of wavelength 4.768 \AA impinged on the interface between the coated surface of the sample wafer and the liquid in the reservoir. The pre-sample collimating slits were chosen to maintain a constant illuminated interfacial area for each measured angle θ , and to prevent the incident beam from illuminating the Viton gasket. The post-sample collimation was chosen to allow the entire reflected beam to impinge on the detector, which was positioned at an angle 2θ relative to the incoming beam direction to measure specular reflection. Each reflectivity curve covered a range in scattering vector $Q_z = 4\pi\lambda^{-1}\sin(\theta)$ from 0.008 to 0.2362 \AA^{-1} .

The reflectivity was calculated as $R = [I(Q_z) - I_B(Q_z)]/I_0(Q_z)$. Here, $I(Q_z)$ is the measured count rate (normalized to a much larger monitor count rate to account for fluctuations in beam intensity). $I_B(Q_z)$ is the background intensity, which arises primarily from incoherent scattering from the liquid reservoir and is calculated by linear interpolation of the backgrounds measured with the detector positioned at 1.5θ and 2.5θ . $I_0(Q_z)$ is the incident beam intensity (also normalized to the monitor count rate) and is directly measured through the silicon substrate at $\theta = 0$ with the detector positioned inline with the incident beam.

2.5.1. Protein incubation for NR. Chilled solutions of detergent-stabilized mVDAC1-GSG-His₆ were diluted with buffer and injected at the desired concentrations into the chilled NR cell (cell temperature 12.8°C). Incubation lasted for 45–60 min before rinsing with buffer and measurement by NR.

2.5.2. Bilayer reconstitution. Diphytanoylphosphatidylcholine (DPhyPC) lipid (Avanti Polar Lipids, Alabaster, Alabama, USA) was lyophilized overnight and dissolved in 0.075% LDAO-containing buffer at a concentration of 0.05 mg ml⁻¹. The lipid solution was injected into the cell and allowed to incubate for 2 h. After incubation, 30 ml of this solution was placed in an external reservoir and combined with about 1.5 g BioBeads SM-2 Resin (Bio-Rad, Hercules, California, USA) with constant stirring. A peristaltic pump was used to circulate this solution through the NR cell, drawing the solution through an inline syringe filter to avoid contamination of the NR cell with the beads. The flow rate was approximately 1 ml min⁻¹ and the cell temperature was maintained at 12.8°C. The dialysis process continued for 3.5 h, after which the NR cell was washed with detergent-free buffer. The solution remaining in the external reservoir did not foam when shaken, indicating substantial removal of the LDAO detergent.

2.5.3. Composition-space modeling. The NR data were modeled using the composition-space modeling procedures described previously (Shekhar *et al.*, 2011). Molecular volumes were estimated from a poly(ethylene glycol) (PEG) density of about 1.2 g cm⁻³, the effective ionic radius of sulfur (Shannon, 1976) and the volume of CH₂ groups (Nagle & Tristram-Nagle, 2000). The thiolated poly(ethylene glycol) tether common to OEG and OEG-NTA was estimated to have a molecular volume of 474 \AA^3 and an average scattering length density of $0.57 \times 10^{-6} \text{\AA}^{-2}$ in H₂O, and the NTA group [(COOH)N(CH₂COO)₂] was estimated to have a volume of 214 \AA^3 , which is consistent with its density of 1.67 g cm⁻³, and average scattering length densities of $2.75 \times 10^{-6} \text{\AA}^{-2}$ in H₂O and $3.24 \times 10^{-6} \text{\AA}^{-2}$ in D₂O. Estimates for the linker between the PEG tether and the NTA group gave a volume of 197.4 \AA^3 and an average scattering length density of $0.60 \times 10^{-6} \text{\AA}^{-2}$. The SAM structure was parameterized by the length of the PEG tether, the length of the PEG–NTA linker and the length of the NTA group. Where necessary, possible NTA oligomerization was modeled using a polymer mushroom model (Milner *et al.*, 1988; Schneck *et al.*, 2013).

2.5.4. Optimizations. Optimization of the composition-space models was performed on the Bridges high-performance computing system (Nystrom *et al.*, 2015; Towns *et al.*, 2014) using the DREAM Markov chain Monte Carlo (MCMC) algorithm (Vrugt *et al.*, 2009) as implemented in the *Bumps* software package (Kienzle *et al.*, 2011). Confidence intervals on parameters and model predictions were calculated from about three million DREAM samples after the optimizer had reached steady state. All fits achieved a χ^2 of less than 1.5, with the exception of the determinations of the structure of 0% and 30% NTA-functionalized SAMs, each of which had a χ^2 of 2.5.

2.6. Surface plasmon resonance

Surface plasmon resonance experiments were carried out as described previously (Vaish *et al.*, 2013) using a Biacore T-100 instrument. SAMs were formed on gold surfaces (Biacore SIA kit Au, GE Healthcare, New York, USA) as described above.

The flow rate was $5 \mu\text{l min}^{-1}$. Response units were not calibrated for this measurement, which was intended only to determine optimal conditions for NR measurements.

2.7. Electrochemical impedance spectroscopy

Electrochemical impedance spectroscopy measurements (Valincius *et al.*, 2012) were performed using a three-electrode configuration in which an Ag/AgCl reference electrode and platinum counter electrode were suspended in buffer above a 0.282 cm^2 patch of gold substrate, which served as a working electrode. The impedance of the SAM was measured from 10 kHz to 1 Hz using a Solartron Analytical ModuLab 2100A potentiostat equipped with a 1 MHz FRA frequency analyzer.

2.8. Molecular dynamics simulations

The protein–membrane simulation systems were built using a *CHARMM-GUI* stepwise protocol (Jo *et al.*, 2008) using the X-ray structure of the VDAC1 channel deposited in the Protein Data Bank (PDB entry 3emn; Ujwal *et al.*, 2008). The simulation system contained one protein embedded into a 1-palmitoyl-2-oleoyl-*sn*-glycero-3-phosphocholine (POPC) bilayer and solvated in a 1 M KCl aqueous solution. The TIP3P water model (Jorgensen *et al.*, 1983) and modified ionic parameters were used in all simulations (Noskov & Roux, 2008; Noskov *et al.*, 2013). The ionization states for all titratable protein residues for simulations at pH 4.0 and pH 7.8 were assigned based on *PROPKA* calculations (Olsson *et al.*, 2011). The systems were next simulated for 300 ns using the *NAMD* program package with the NPT ensemble in the orthorhombic box and the CHARMM36 force field for lipids and protein atoms (Best *et al.*, 2012; Pastor & MacKerell, 2011; Essmann *et al.*, 1995). The particle-mesh Ewald summation was used to calculate electrostatic forces (Essmann *et al.*, 1995). All equilibration runs were performed with a time step

of 2 fs. The fully equilibrated structures were used to seed production simulations with the *ANTON2* platform (Shaw *et al.*, 2014). The production runs were for $2.5 \mu\text{s}$ each with the CHARMM36 force field. The production runs were executed in a semi-isotropic (NP α T) ensemble at a temperature of 315 K maintained by the Nosé–Hoover thermostat. The time step for production runs was set to 2 fs and trajectories were saved every 240 ps. Nonbonded and long-range electrostatic interactions were evaluated every 2 and 6 fs, respectively. Long-range electrostatics were calculated by the *k*-Gaussian Ewald method (Shan *et al.*, 2005) with a $64 \times 64 \times 64$ grid. *SHAKE* was used to constrain all bonds involving H atoms. All of the trajectory analysis was performed using the *CHARMM* program package.

3. Results and discussion

3.1. Formation of ptBLMs

The scheme for forming ptBLMs is described in Section 2 and shown in Fig. 1. A silicon substrate is coated with a thin ($\sim 20 \text{ \AA}$) adhesion layer followed by $\sim 150 \text{ \AA}$ of gold. The self-assembled monolayer (SAM) is a dense layer of ethylene glycol hexamers, an adjustable fraction of which is functionalized with nickel-charged NTA groups attached to the gold surface using thiol chemistry (Fig. 1a).

Detergent-stabilized recombinant murine VDAC1 with a C-terminal hexahistidine affinity tag (mVDAC1-GSG-His₆) is then presented to the charged NTA surface (Fig. 1b), resulting in selective binding. Importantly, the histidine tag is attached to the C-terminus of VDAC, because the N-terminal α -helix is sequestered inside the channel and may be involved in the (as yet unknown) mechanism of VDAC gating (Noskov *et al.*, 2016; Villinger *et al.*, 2010; Choudhary *et al.*, 2010; Rappaport *et al.*, 2015). The C-terminus, in contrast, is thought to play a

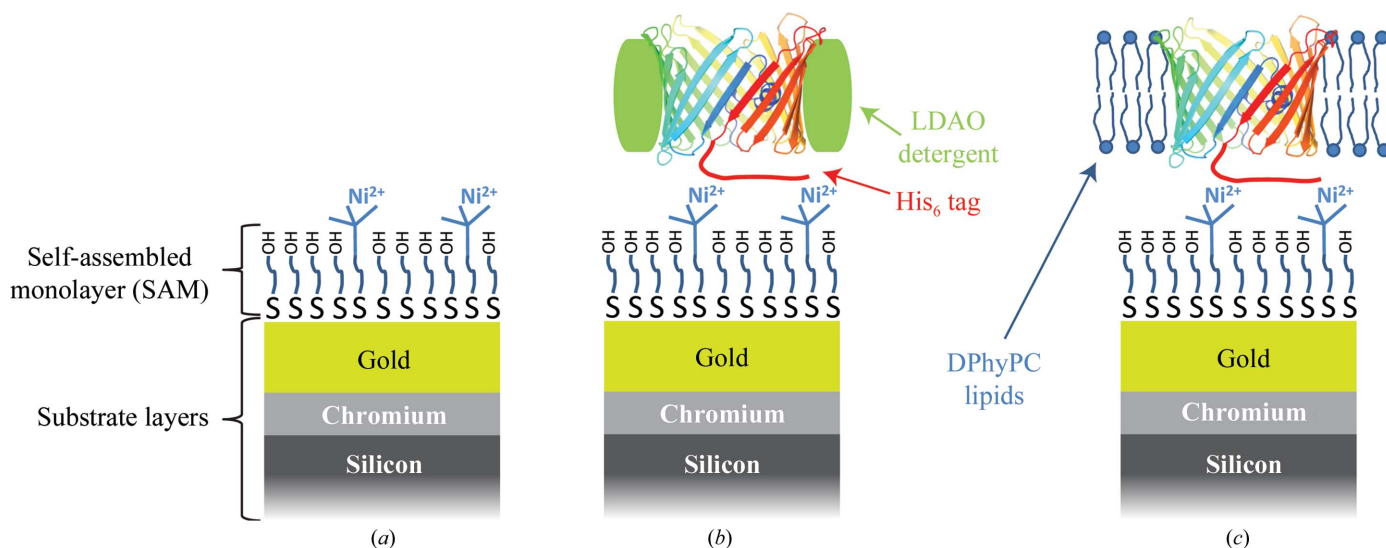


Figure 1

Schematic of the formation of a protein-tethered bilayer lipid membrane. The VDAC structure is from Ujwal *et al.* (2008). (a) A sparsely functionalized NTA surface is created from the adsorption of thiols onto a gold substrate and charged with nickel ions. (b) Detergent-stabilized mVDAC1-GSG-His₆ is captured onto the self-assembled monolayer (SAM). (c) The detergent is replaced by the desired lipid (in this case DPhyPC) by dialysis.

purely structural role and is more exposed to the membrane surface.

Finally, the detergent is replaced with lipid by dialysis (Fig. 1c). For this purpose, diphytanoylphosphatidylcholine was chosen for consistency with electrophysiological experiments on VDAC reconstituted into ‘free’ planar membranes (Gurnev *et al.*, 2011; Teijido *et al.*, 2012; Eddy *et al.*, 2015; Rostovtseva *et al.*, 2015). DPhyPC is often a preferable lipid choice for these experiments owing to the stability of bilayers made of this lipid and the robust process of VDAC reconstitution. Importantly, using a magic angle spinning NMR spectroscopy study it was shown that backbone structures of

VDAC1 reconstituted in DPhyPC and of the protein reconstituted in dimyristoylphosphatidylcholine are nearly identical (Eddy *et al.*, 2012).

The following sections contain a detailed structural analysis of the NTA-functionalized SAM, the surface-immobilized detergent-stabilized mVDAC1-GSG-His₆ and the reconstituted bilayer. We also show the effect of a manipulation of the ptBLM to pH 4.1, mimicking cytosolic acidification in pathologies that are associated with a total or partial lack of oxygen supply (anoxia or hypoxia, respectively), such as ischemia/reperfusion injury (Lemasters *et al.*, 1996; Murphy & Steenbergen, 2008).

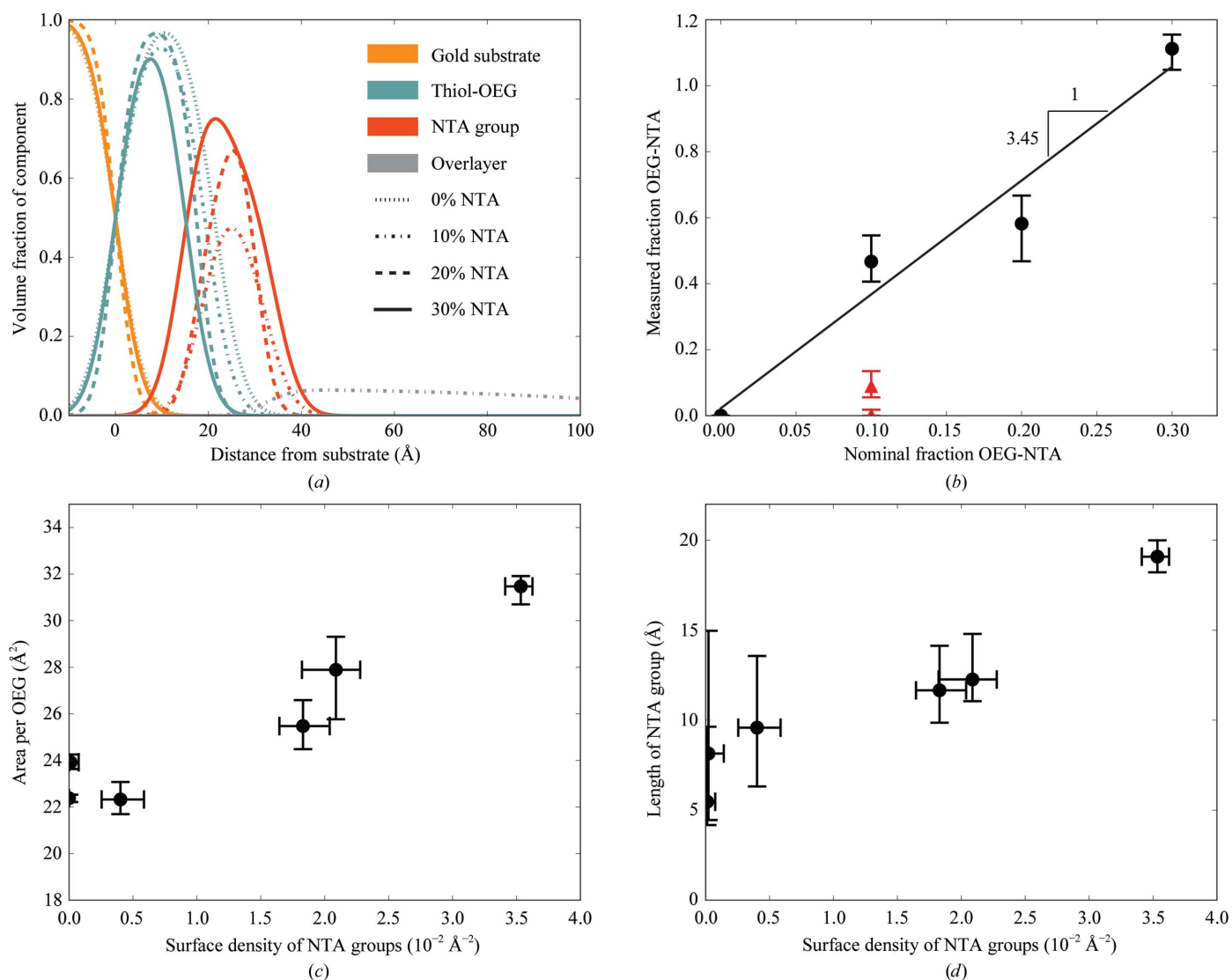


Figure 2 NR structural determination of NTA-functionalized OEG SAMs. (a) Volume fractions of OEG and NTA molecular components for different SAM compositions. Labels correspond to the nominal percentage of NTA. The OEG groups thin, and the NTA groups thicken, with increasing surface NTA density. The overlayer was required to fit the 10% NTA data and probably represents oligomerization of OEG-NTA. (b) A higher fraction of OEG-NTA is present on the surface than expected from the as-prepared solutions. The actual mole fraction of OEG-NTA is 3.45 times the as-prepared mole fraction, as determined from the slope of the (unweighted) best-fit line to the measured mole fraction versus the as-prepared mole fraction of OEG-NTA. Subsequent experiments using a 10% nominal OEG-NTA mole fraction yielded lower surface coverages (red diamonds). (c) The area per OEG molecule, as deduced from the estimated molecular volume and the measured thickness of the OEG layer, increases with the measured fraction of surface NTA. (d) The NTA group conformation depends on the surface density. NTA groups are extended at higher surface density, as expected for a mushroom-to-brush transition. All error bars are calculated from statistical analysis of Monte Carlo optimization results and represent 95% confidence intervals.

The sensitivity of reconstituted VDAC channels to the applied voltage depends on the charged residues that form the ‘voltage sensor’. Low pH neutralizes acidic charges and thus increases the net positive charge involved in gating, meaning that lower voltages are required to close the channel (Teijido *et al.*, 2014). All of the observed effects of pH on VDAC gating obtained by electrophysiology (Teijido *et al.*, 2014) or by structural circular-dichroism measurements (Mannella, 1998; Shao *et al.*, 1996) are completely reversible.

3.2. Structure of OEG-NTA self-assembled monolayers

The structure of the OEG-NTA monolayers was determined by NR. NR data were collected for surfaces incubated with 0.2 mM thiolated OEG solutions containing nominal mole fractions of NTA-terminated OEG of 0%, 10%, 20% and 30%. The remainder was hydroxy-terminated OEG. The reflectivity data were optimized to a composition-space model, as described in Section 2. Neutron scattering length densities for the OEG groups, the OEG-NTA linker and the NTA group were calculated from the known elemental compositions and estimated molecular volumes and were fixed for the optimization. The results of the model optimization are shown in Fig. 2. For reflectivity curves and model fits, see Supplementary Figs. S1–S4.

Fig. 2(a) shows a representation of the volume occupancy of the molecular components of the OEG-NTA SAM for different mole fractions of OEG/OEG-NTA. Interestingly, the thickness of the OEG layer decreases with the OEG-NTA fraction. Given the known molecular volume of the OEG segment, the area per OEG molecule can be extracted (Fig. 2c); the result confirms previous measurements (20–25 Å² per OEG molecule) using transmission electron microscopy of gold nanoparticles coated with thiolated OEG tethers of similar length (Hinterwirth *et al.*, 2013).

By comparing the total volumes of the OEG and NTA layers, we determine the actual fraction of OEG-NTA molecules present in the SAM (Fig. 2b). Remarkably, the measured fraction is three times larger than the as-prepared mole fraction as determined from the slope of the (unweighted) best-fit line shown in Fig. 2(b). The enhancement of OEG-NTA on the surface suggests a stabilizing interaction between the NTA headgroups that is sufficient to overcome the energy cost of creating an OEG layer that is thinner and sparser than it would be without the NTA (Fig. 2c). Curiously, this is the opposite effect to that previously reported (Vaish *et al.*, 2013), although in later measurements using the same preparations of thiols the surface coverage with NTA was significantly less (red diamonds in Fig. 2b).

Finally, the morphology of the NTA layer changes significantly with NTA surface density. Fig. 2(d) shows the relationship between the surface density and length of the NTA groups. As the surface density increases, the length also increases. This is consistent with a mushroom-to-brush transition (Kuhl *et al.*, 1994). The lateral pressure, which presumably results from the steric (entropic) repulsion of neighboring NTA groups, is also responsible for the increased

area per OEG molecule. This repulsion is probably enhanced by the buffer conditions used in these experiments, where the electrostatic interaction length is on the order of the separation between the charged NTA groups.

A low volume fraction overlayer is required to fit the 10% NTA film data. We hypothesize that this is owing to oligomerized OEG-NTA, which may occur with very small quantities of oxidant (to create dithiol bonds) and divalent ions

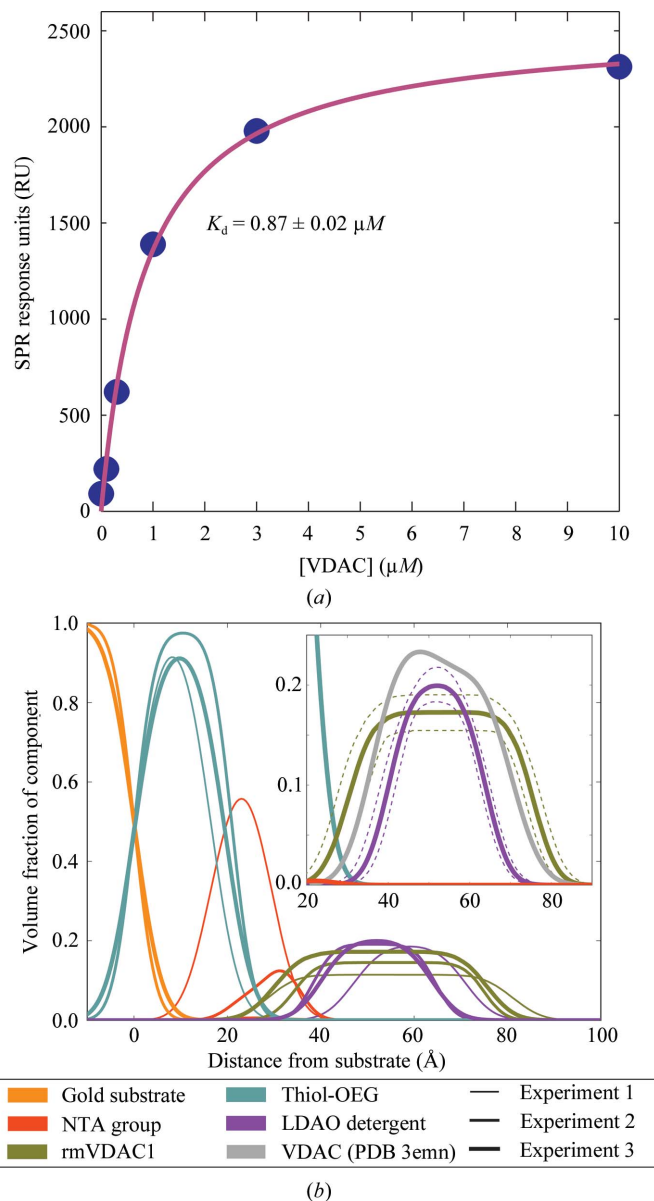


Figure 3

Capture of mVDAC1-GSG-His₆ (rmVDAC1) onto an NTA-functionalized surface. (a) Surface plasmon resonance data showing a binding affinity to the surface of about 1 μM. (b) Structure of the surface-captured, detergent-stabilized VDAC as determined by NR in three independent experiments, which are distinguished by different line weights. The surface density of protein is comparable in all cases. Inset: detail of the protein and detergent density profiles for experiment 3, showing 95% confidence intervals and comparing experimental data with the protein density profile calculated from the crystal structure of mVDAC1 (PDB entry 3emn) oriented with the pore axis normal to, and the C-terminus proximal to, the substrate.

Table 1

Measured quantities from the binding of LDAO–VDAC complexes to NTA SAMs.

Ranges are 95% confidence intervals as calculated by the *DREAM* optimization algorithm.

Quantity	Experiment 1	Experiment 2	Experiment 3
In-plane packing density	0.302 ^{+0.020} _{-0.017}	0.337 ^{+0.016} _{-0.017}	0.374 ^{+0.025} _{-0.019}
NTA:protein molar ratio	122 ⁺²⁴ ₋₁₈	26.3 ^{+9.3} _{-7.3}	1.1 ^{+7.2} _{-1.0}
LDAO:protein volumetric ratio	0.77 ^{+0.19} _{-0.13}	0.86 ^{+0.16} _{-0.13}	0.63 ^{+0.16} _{-0.12}
LDAO:protein molar ratio	62 ⁺¹⁵ ₋₁₁	68 ⁺¹³ ₋₁₁	50.2 ^{+12.4} _{-9.3}
Detergent thickness (Å)	23.9 ^{+2.1} _{-2.5}	26.0 ^{+1.5} _{-1.9}	23.7 ^{+3.5} _{-3.5}
Protein thickness (Å)	51.1 ^{+2.9} _{-3.9}	39.8 ^{+3.6} _{-3.7}	44.2 ^{+4.4} _{-6.0}

(to coordinate the NTA groups). Accordingly, we model the overlayer as a polymer in a mushroom configuration with a parabolic density profile (Milner *et al.*, 1988; Schneck *et al.*, 2013). The volume fraction, maximum extent and scattering length density of the overlayer were left as free parameters in the optimizations and were determined to be 0.0672^{+0.0051}_{-0.0042}, 118.6^{+4.9}_{-5.5} and -0.446^{+0.258}_{-0.052}, respectively (the ranges are 95% confidence intervals). Attempts to remove this overlayer were not successful. In particular, treatment with 100 mM EDTA only reduced the volume of the overlayer by about 25%.

3.3. Adsorption of VDAC to the NTA SAM

The affinity of mVDAC1-GSG-His₆ for the NTA-functionalized surface was determined using surface plasmon resonance. Fig. 3(a) shows the binding curve of mVDAC1-GSG-His₆ to 10% OEG-NTA/90% OEG SAM, as determined by surface plasmon resonance using a Biacore T-100 instrument. The affinity is approximately 1 μM, which is somewhat weaker than expected from the hexahistidine tag (Knecht *et al.*, 2009), but is similar to previous measurements with hexahistidine-tagged probes binding to multiple NTA groups (Lata *et al.*, 2005). The accessibility of the hexahistidine tag to the surface is also unknown.

3.4. Structure of surface-captured VDAC

The structure of detergent-stabilized, NTA-bound VDAC was determined using NR, as shown in Fig. 3(b). For reflectivity curves and model fits, see Supplementary Figs. S5–S7. The data were modeled with two additional (overlapping) molecular components representing the protein and the detergent. The average scattering length densities of the protein were 1.935 × 10⁻⁶ and 3.266 × 10⁻⁶ Å⁻² in H₂O and D₂O, respectively (as estimated from the amino-acid sequence) and that of the LDAO detergent was -0.179 × 10⁻⁶ (calculated from the elemental composition and the molecular volume as determined from the physical density). Three independent experiments are shown, with a broad range of observed surface NTA densities. For experiments 1 and 2 VDAC was deposited at 1 μM, while for experiment 3 it was deposited at 2 μM. Interestingly, the amount of protein on the surface does not depend strongly on the surface density of NTA, suggesting that a relatively sparse coverage of NTA groups is sufficient to bind the protein. Instead, the density

appears to be determined more strongly by packing-density considerations. The maximum in-plane random packing density of protein–detergent complexes is about 0.6 (Gotoh & Finney, 1974). As shown in Table 1, we observe about half of this maximum density (ranges are 95% confidence intervals). This is consistent with the use of a protein concentration around the equilibrium binding constant, for which we expect about half the maximum density. For each of the three experiments, the surface density of the NTA headgroups is greater than the density of protein molecules, *i.e.* the observed molar ratio of NTA to protein shows that within the measurement uncertainty there is sufficient NTA density to bind the proteins in each experiment (see Table 1) with multiple NTA molecules per protein.

Interestingly, in experiment 1, with the highest NTA surface density, both the protein and detergent are found at a larger distance from the surface. This is presumably owing to the additional length of the NTA headgroups (Fig. 2d).

The NR results allow estimation of the average properties of the detergent–VDAC complex, as reported by volumetric and molar ratios of LDAO to VDAC. As shown in Table 1, each VDAC binds approximately 60 LDAO molecules. This is comparable to, if somewhat less than, other membrane proteins, but is consistent with the smaller detergent concentration required to stabilize VDAC (0.041 mM compared with ~1 mM for other protein–detergent complexes; Chaptal *et al.*, 2017). For comparison, the typical number of molecules in an LDAO micelle is about 70 (Thiyagarajan & Tiede, 1994; Timmins *et al.*, 1988).

The physical dimensions of the LDAO and VDAC components are also listed in Table 1. The thickness of the detergent layer is quite consistent across the three experiments at about 25 Å. This thickness is intermediate to the major and minor axes of prolate spheroidal LDAO micelles (30.6 and 19.4 Å, respectively; Thiyagarajan & Tiede, 1994). It is also somewhat thinner than the 27–28 Å hydrophobic thickness expected from the typical model lipids (POPC and DPhyPC) used to mimic the mitochondrial outer membrane (Kučerka *et al.*, 2011).

The protein profile is somewhat longer than expected from the crystal structure (PDB entry 3emn; Ujwal *et al.*, 2008). The inset in Fig. 3 compares the protein and detergent profiles using ‘box’ models, as before, and the profile calculated from the crystal structure when the VDAC is oriented with the pore axis normal, and the C-terminus proximal, to the surface. The full width at half maximum of the calculated profile (smoothed with a Gaussian filter) is 33.6 Å, about 10 Å shorter than that measured experimentally. This may indicate that the protein adopts an elongated configuration in detergent or does not sit at a uniform distance from the substrate surface, or some combination of the two, resulting in protein tilt or elongation (Kozuch *et al.*, 2014). We also cannot rule out a population of nonspecifically adsorbed VDAC; previous studies have shown that using a low (nominally 10%) NTA surface concentration (Jagalski *et al.*, 2015) and reduced temperature (Vaish *et al.*, 2013) reduces, but does not completely eliminate, nonspecific adsorption.

3.5. Structure of VDAC reconstituted into DPhyPC bilayers

After reconstitution with DPhyPC and removal of the LDAO detergent by dialysis (see Section 2), the structure of the VDAC-tethered bilayers was determined by NR. The data were then modeled by holding the shape (but not the distance from the substrate) of the protein density profile constant and assuming that all of the protein is reconstituted into the bilayer (*i.e.* none is lost to denaturation and the detergent is completely removed by the reconstitution procedure). A

composition-space model of a floating lipid bilayer (Shekhar *et al.*, 2011) comprised an organized set of six molecular components of different scattering length densities representing the inner headgroups, inner acyl chains, inner terminal methyl groups, outer terminal methyl groups, outer acyl chains and outer headgroups. The entire bilayer model incorporates known data regarding the volumes of these various groups for DPhyPC and is thus parameterized by only three quantities: the position of the bilayer relative to the protein, the area fraction of the surface occupied by the bilayer (represented in this case by the space left after all other molecular components have been accounted for) and the thickness of the acyl chains. The acyl-chain thickness determines the total bilayer thickness, the thickness of the hydrophobic region, the area per lipid and the area density of the headgroups. A freeform model, implemented as a Catmull–Rom spline, was also included above the bilayer to account for the significant amount of lipid that is left on the surface after the reconstitution process.

The results of this fitting for experiment 3 are shown in Fig. 4 (for reflectivity curves and model fits, see Supplementary Fig. S8). Fig. 4(*a*) shows the molecular composition immediately after reconstitution, including the bilayer and the excess lipid. A number of physical quantities can be immediately extracted from these results. The thickness of the acyl chains is $13.33^{+0.04}_{-0.43}$ Å, which corresponds to an area per lipid of $74.8^{+2.5}_{-2.2}$ Å². This is in excellent agreement with previously measured quantities for fluid-phase DPhyPC bilayers, particularly when the temperature dependence of the bilayer structure is accounted for (Kučerka *et al.*, 2011). If a significant amount of detergent were present, we would expect deviation from this value, leading us to conclude that little detergent is left. In future NR experiments this could be verified using deuterated lipid or detergent (Jagalski *et al.*, 2015).

The area fraction of water remaining in the bilayer was measured to be $0.164^{+0.030}_{-0.037}$. From the structure of the detergent-stabilized, surface-captured VDAC, and the estimated $34\,098$ Å³ volume of VDAC (see Supplementary Fig. S10 and Table S2), the area per VDAC molecule can be calculated to be $4.50^{+0.67}_{-0.49} \times 10^3$ Å². Over the bilayer thickness, the VDAC lumen has an average area of approximately 412 Å², as determined from MD simulations (see Supplementary Fig. S10 and Table S2). Thus, we expect the water content of a complete VDAC-tethered bilayer to be approximately 0.092. We thus have approximately twice as much water in the bilayer as we expect. The presence of significant amounts of excess lipid above the bilayer suggests the possible presence of unruptured vesicles, which may contribute to the presence of additional water in the bilayer region.

A previous NR study of ptBLMs using the leucine transporter reported a surface coverage of only 45% and found that each leucine transporter protein was associated with about 52 lipids (Jagalski *et al.*, 2015). The average protein area of 972 Å² over the bilayer thickness (see Supplementary Fig. S10 and Table S2) can be estimated from the protein structure. Using the area per VDAC molecule, the average lumen area of 412 Å² and this value, and assuming the remaining area to be

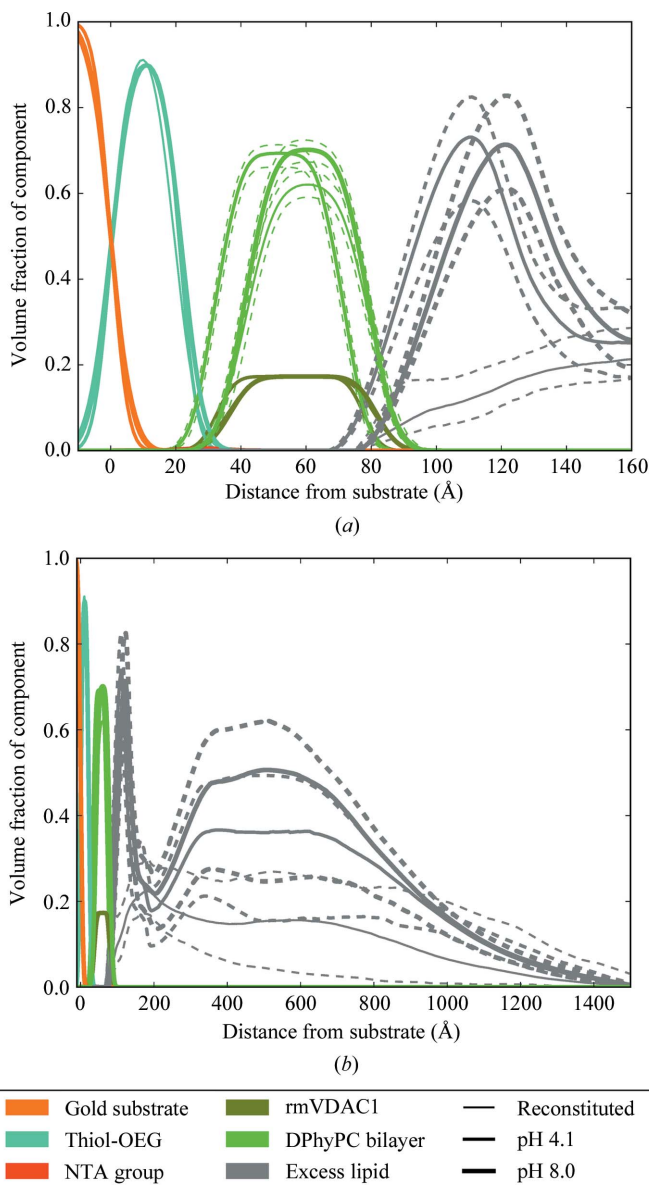


Figure 4
Structure of the bilayer as reconstituted at pH 4.1 and after returning to pH 8.0. (*a*) Detail of the reconstituted bilayer structure. The total protein and protein length were held constant for this measurement, but the positions of the protein and bilayer were allowed to vary independently. (*b*) Excess lipid profiles at large distances from the substrate, suggesting the presence of unruptured vesicles on the surface. Dashed lines represent 95% confidence intervals on the bilayer and excess lipid profiles.

filled with lipid, we arrive at $42_{\pm 9}^{\pm 9}$ lipids per VDAC molecule, which is in good agreement with the previous result. This suggests that the stabilizing lipid belt around proteins in ptBLMs does not, in general, extend far from the protein, and a significant protein density is therefore required to create a complete ptBLM. Importantly, the previous study used a very different dialysis procedure, indicating that ptBLM formation is not very sensitive to the dialysis method.

3.6. ptBLM structural changes at low pH

The conventional means of inducing VDAC gating is the application of a transmembrane potential (Colombini, 1989; Zimmerberg & Parsegian, 1986; Colombini *et al.*, 1996; Rappaport *et al.*, 2015). In principle, this is experimentally feasible by coupling electrodes to the gold substrate and to the electrolyte; in practice, the electrode surface resistance, particularly between the gold and the electrolyte, is much larger than the resistance of the VDAC perforated bilayer, and it is not possible to achieve a significant voltage drop across the bilayer. The conductance of a VDAC channel in 150 mM NaCl is approximately 0.5 nS. At one VDAC molecule per 5000 \AA^2 , the conductance per area of the bilayer is approximately 1000 S cm^{-2} . In contrast, the conductance of the OEG-NTA SAM was determined to be less than $10^{-5} \text{ S cm}^{-2}$ by electrostatic impedance spectroscopy (see Supplementary Fig. S11). This limitation is not unique to the ptBLM system; in an experiment in which VDAC was delivered to an electrode surface using proteoliposomes, the resistance of the bilayer was measured to be more than two orders of magnitude smaller than the combined resistance of the electrode surface and submembrane space (Kozuch *et al.*, 2014).

Instead, we use the fact that the sensitivity of the VDAC channels to voltage is significantly increased by acidification (Teijido *et al.*, 2014; Ermishkin & Mirzabekov, 1990; Bowen *et al.*, 1985). In conjunction with the anecdotal observation that the VDAC channels, if held for long periods of time in a closed state, can become irreversibly closed, we simply cycled the reconstituted bilayer between pH 8 and pH 4.1 until a steady state was achieved, *i.e.* the measured NR spectra of the bilayers at pH 4.1 and pH 8 were unchanged from prior measurements at the same pH value. We then measured the structure of the bilayer at pH 4.1 and subsequently at pH 8.

The results of this experiment are shown in Fig. 4, in comparison to the bilayer structure immediately following reconstitution (for reflectivity curves and model fits, see Supplementary Fig. S9). Two major differences among the three structures are immediately apparent. Firstly, the water occupancy of the bilayer is decreased to $0.0980_{-0.023}^{+0.029}$ (95% confidence intervals) at pH 4.1; upon restoring the pH to 8 the water occupancy is $0.0835_{-0.023}^{+0.033}$ and thus is not restored to its original value. Note that both values of the water occupancy of the bilayer match the estimate of 0.084 for a complete bilayer with open VDAC channels very well. This suggests that the manipulations of the bilayer in cycling the bilayer between pH 4.1 and 8 actively ‘healed’ the bilayer or simply allowed sufficient time for the bilayer to come to a complete state.

An alternative explanation is that the decrease in water content of the bilayer is owing to large structural changes upon gating of the VDAC channel, which is enhanced at low pH. In this interpretation, the observed decrease in the volume of the pore lumen is 44%, which is consistent with the observed change in conductivity of the VDAC channel upon gating at low pH (Teijido *et al.*, 2014). Large volume changes have also been surmised from thermodynamic estimates (Zimmerberg & Parsegian, 1986). In this view, the failure of the channels to reopen upon increasing the pH back to 8 is owing to permanent closure owing to the long measurement times at pH 4.1 (VDAC channels reconstituted into planar lipid bilayers under gating conditions such as low pH and/or high voltage often transition into an indefinitely long-lived closed state). However, MD simulations show a change in pore lumen volume of only 5–6% without applied voltage. Thus, we suspect that the decreased water content of the bilayer is owing to improved reconstitution of the VDAC during the pH-cycling process, although in the absence of detailed knowledge of the local fields experienced by the VDAC molecule it is difficult to conclusively distinguish the two possibilities.

The second major pH-dependent change that can be observed in Fig. 4 is that at pH 4.1 the entire bilayer moves about 10 \AA closer to the substrate. We imagine this to be owing to changes in the electrostatic and repulsive hydration forces in the submembrane space upon titration of the VDAC polyhistidine affinity tag, but do not otherwise have a compelling explanation. Curiously, low pH can be used to elute from a Ni-NTA surface (Bornhorst & Falke, 2000); in the presence of the bilayer, van der Waals and other attractive forces (Anderson *et al.*, 2009) appear to play a significant role and maintain the affinity between the protein-tethered bilayer and the substrate. This result is confirmed by the fact that in a different experiment, rinses with imidazole at up to 1 M concentration did not have a significant effect on the structure of the protein-tethered bilayer, much less dissociate it from the substrate.

Interestingly, the free-form model of the excess lipid appears to indicate the presence of a second bilayer forming above the protein-tethered bilayer. The scattering length density of this region does not indicate the presence of any protein, as expected. The presence of excess lipid complicates the models required to fit hypothetical NR data in the presence of cytosolic binding partners to the bilayer-tethering integral membrane proteins. Because the neutron scattering length density of protein is so different from that of lipids, the protein and lipid components can be separated by NR, but at the cost of structural sensitivity. For other less specific surface techniques excess lipid may play an even more confounding role. This result suggests that future experiments may benefit from a lower concentration of lipid during the dialysis process to avoid the accumulation and subsequent reorganization of excess lipid structures above the bilayer of interest. Counter-intuitively, rinses with mixtures of up to 40% ethanol in buffer served only to facilitate this rearrangement into multilayer structures, while the surface-proximal bilayer completeness remained unchanged within measurement error.

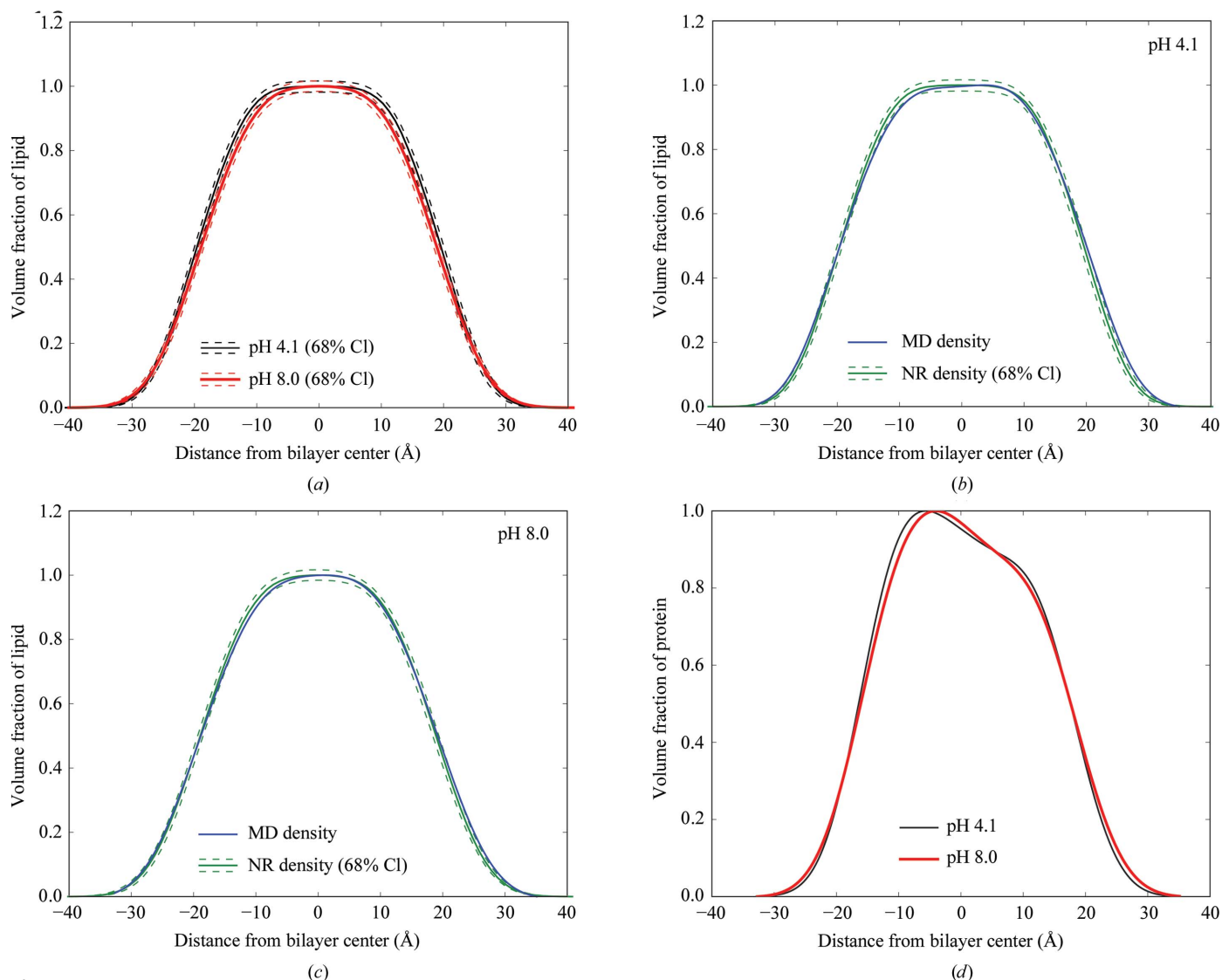


Figure 5

Comparison of lipid-bilayer volume occupancy profiles as determined by NR and MD simulations. (a) Comparison of pH 4.1 and pH 8.0 using NR. 68% confidence intervals are shown by dashed lines. Note the change in bilayer thickness at low pH. (b, c) Comparison of measured NR lipid densities to MD at pH 4.1 (b) and pH 8.0 (c). (d) Protein density profiles as determined by MD do not change significantly with pH.

3.7. Comparison with MD simulations

Fig. 5 shows the lipid-bilayer volume density profiles as measured by NR and MD, and scaled as if there were no protein in the bilayer. Interestingly, we observe that the thickness of the lipid bilayer increases by about 2 Å at pH 4.1 (Fig. 5a) and reversibly decreases again at pH 8. The same effect can be seen in the lipid density profiles generated by the MD simulations (Figs. 5b and 5c). Thickening of phosphatidylcholine bilayers at low pH has been observed in previous simulations (Lähdesmäki *et al.*, 2010), although experimental confirmation of this has not, to the best of our knowledge, been reported to date. In this case the MD simulations provide an important clue. Constant-pH MD simulations with explicit treatment of all ionizable groups, while conceptually feasible, remain prohibitively slow for the purposes of this study (Chen *et al.*, 2016; Radak *et al.*, 2017). To include the effect of pH in classical MD simulations we chose to titrate the appropriate

residues on the VDAC channel, leaving the charge state of the phosphatidylcholine headgroups unchanged. The MD simulations do not show a significant change in the protein density profile at low pH (Fig. 5d). Thus, the observed membrane thickening is likely to be an effect of the altered electrostatic interaction between the VDAC channel and the lipid headgroups, rather than being an intrinsic property of the bilayer itself (Mlayeh *et al.*, 2017). In both the NR experiments and MD simulations the protein is present at high density, which is evidently sufficient to alter the bilayer geometry at low pH.

4. Conclusions

We provide a comprehensive structural characterization of each step in the formation of a ptBLM. The structure of the NTA-functionalized SAM depends on the surface coverage of NTA groups, which has implications for the specificity and

efficiency of NTA column purification techniques. Hexahistidine-tagged VDAC molecules stabilized in LDAO detergent micelles adopt a conformation on the surface consistent with capture of the histidine tag by the nickel-charged NTA-functionalized SAM. Finally, lipid reconstitution of the captured VDAC channels results in complete bilayer formation. Importantly, the NR data show that the reconstitution process is very slow and can result in a significant amount of excess lipid at the surface. Finally, NR shows subtle changes in the bilayer thickness and separation from the substrate at low pH that yield insights into the lipid–protein interactions. These results demonstrate the suitability of the ptBLM system for reconstituting integral membrane proteins at high density for structural analysis by NR and other surface-sensitive techniques. Most importantly for future studies, the protein density and bilayer completeness are sufficient to introduce soluble binding partners to the tethering integral membrane proteins and determine their structures.

Acknowledgements

The authors wish to thank Sergey Bezrukov for discussions and comments on the manuscript. They also thank Amit Vaish, Dan Scott and Sushil Satija for technical support, David Vanderah for the kind gift of the thiol molecules and Seonghoon Kim and Wonpil Im for generously sharing scripts and numerical receipts for *ANTON2* simulations. We acknowledge the National Institute of Standards and Technology, US Department of Commerce, for providing the neutron research facilities used in this work. Samples were fabricated in part by Matthew Robinson at the NIST Center for Nanoscale Systems nanofabrication facility. Certain commercial materials, equipment and instruments are identified in this work to describe the experimental procedure as completely as possible. In no case does such an identification imply a recommendation or endorsement by NIST, nor does it imply that the materials, equipment or instrument identified are necessarily the best available for the purpose.

Funding information

This work used the Extreme Science and Engineering Discovery Environment (XSEDE), which is supported by National Science Foundation grant ACI-1053575. Specifically, it used the Bridges system, which is supported by NSF award No. ACI-1445606, at the Pittsburgh Supercomputing Center (PSC). Anton 2 computer time (PSCA17051P) was provided by the Pittsburgh Supercomputing Center (PSC) through grant R01GM116961 from the National Institutes of Health. The Anton 2 machine at PSC was generously made available by D. E. Shaw Research. DPH was supported by a National Academies of Sciences NIST/NIH Joint Research Associate-ship. TKR was supported by the Intramural Research Program of the Eunice Kennedy Shriver National Institute of Child Health and Human Development, NIH. AK and SKB were supported by the Intramural Research Program of the National Institute for Diabetes and Digestive and Kidney Diseases. SYN was supported by the Natural Sciences and

Engineering Research Council of Canada (NSERC grant No. RGPIN-315019) and the Alberta Innovates Technical Futures Strategic Chair in Bio-Molecular Simulations.

References

- Almén, M. S., Nordström, K. J., Fredriksson, R. & Schiöth, H. B. (2009). *BMC Biol.* **7**, 50.
- Anderson, T. H., Min, Y., Weirich, K. L., Zeng, H., Fygenson, D. & Israelachvili, J. N. (2009). *Langmuir*, **25**, 6997–7005.
- Aslanidis, C. & de Jong, P. J. (1990). *Nucleic Acids Res.* **18**, 6069–6074.
- Ataka, K., Giess, F., Knoll, W., Naumann, R., Haber-Pohlmeier, S., Richter, B. & Heberle, J. (2004). *J. Am. Chem. Soc.* **126**, 16199–16206.
- Bayrhuber, M., Meins, T., Habeck, M., Becker, S., Giller, K., Villinger, S., Vonrhein, C., Griesinger, C., Zweckstetter, M. & Zeth, K. (2008). *Proc. Natl Acad. Sci. USA*, **105**, 15370–15375.
- Berg, O. G. & von Hippel, P. H. (1985). *Annu. Rev. Biophys. Biophys. Chem.* **14**, 131–158.
- Bertram, N., Laursen, T., Barker, R., Bavishi, K., Møller, B. L. & Cárdenas, M. (2015). *Langmuir*, **31**, 8386–8391.
- Best, R. B., Zhu, X., Shim, J., Lopes, P. E., Mittal, J., Feig, M. & MacKerell, A. D. Jr (2012). *J. Chem. Theory Comput.* **8**, 3257–3273.
- Bornhorst, J. A. & Falke, J. J. (2000). *Methods Enzymol.* **326**, 245–254.
- Bowen, K. A., Tam, K. & Colombini, M. (1985). *J. Membr. Biol.* **86**, 51–59.
- Braun, A. R., Lacy, M. M., Ducas, V. C., Rhoades, E. & Sachs, J. N. (2014). *J. Am. Chem. Soc.* **136**, 9962–9972.
- Bronder, A. M., Bieker, A., Elter, S., Eitzkorn, M., Häussinger, D. & Oesterhelt, F. (2016). *Biophys. J.* **111**, 1925–1934.
- Castellana, E. T. & Cremer, P. S. (2006). *Surf. Sci. Rep.* **61**, 429–444.
- Chaptal, V., Delolme, F., Kilburg, A., Magnard, S., Montigny, C., Picard, M., Prier, C., Monticelli, L., Bornert, O., Agez, M., Ravaut, S., Orelle, C., Wagner, R., Jawhari, A., Broutin, I., Pebay-Peyroula, E., Jault, J.-M., Kaback, H. R., le Maire, M. & Falson, P. (2017). *Sci. Rep.* **7**, 41751.
- Chen, W., Huang, Y. D. & Shen, J. N. (2016). *J. Phys. Chem. Lett.* **7**, 3961–3966.
- Choudhary, O. P., Ujwal, R., Kowallis, W., Coalson, R., Abramson, J. & Grabe, M. (2010). *J. Mol. Biol.* **396**, 580–592.
- Colombini, M. (1989). *J. Membr. Biol.* **111**, 103–111.
- Colombini, M. (2004). *Mol. Cell. Biochem.* **256–257**, 107–115.
- Colombini, M., Blachly Dyson, E. & Forte, M. (1996). *Ion Channels*, edited by T. Narahashi, pp. 169–202. New York: Plenum Press.
- Eddy, M. T., Andreas, L., Tejjido, O., Su, Y., Clark, L., Noskov, S. Y., Wagner, G., Rostovtseva, T. K. & Griffin, R. G. (2015). *Biochemistry*, **54**, 994–1005.
- Eddy, M. T., Ong, T. C., Clark, L., Tejjido, O., van der Wel, P. C., Garces, R., Wagner, G., Rostovtseva, T. K. & Griffin, R. G. (2012). *J. Am. Chem. Soc.* **134**, 6375–6387.
- Ermishkin, L. N. & Mirzabekov, T. A. (1990). *Biochim. Biophys. Acta*, **1021**, 161–168.
- Essmann, U., Perera, L., Berkowitz, M. L., Darden, T., Lee, H. & Pedersen, L. G. (1995). *J. Chem. Phys.* **103**, 8577–8593.
- Fragneto, G., Charitat, T., Graner, F., Mecke, K., Perino-Gallice, L. & Bellet-Amalric, E. (2001). *Europhys. Lett.* **53**, 100–106.
- Früh, V., IJzerman, A. P. & Siegal, G. (2011). *Chem. Rev.* **111**, 640–656.
- Fusco, G., De Simone, A., Gopinath, T., Vostrikov, V., Vendruscolo, M., Dobson, C. M. & Veglia, G. (2014). *Nature Commun.* **5**, 3827.
- Giess, F., Friedrich, M. G., Heberle, J., Naumann, R. L. & Knoll, W. (2004). *Biophys. J.* **87**, 3213–3220.
- Gotoh, K. & Finney, J. L. (1974). *Nature (London)*, **252**, 202–205.
- Gurnev, P. A., Rostovtseva, T. K. & Bezrukov, S. M. (2011). *FEBS Lett.* **585**, 2363–2366.
- Hiller, S., Garces, R. G., Malia, T. J., Orekhov, V. Y., Colombini, M. & Wagner, G. (2008). *Science*, **321**, 1206–1210.

- Hinterwirth, H., Kappel, S., Waitz, T., Prohaska, T., Lindner, W. & Lämmerhofer, M. (2013). *ACS Nano*, **7**, 1129–1136.
- Hodge, T. & Colombini, M. (1997). *J. Membr. Biol.* **157**, 271–279.
- Hoogerheide, D. P., Noskov, S. Y., Jacobs, D., Bergdoll, L., Silin, V., Worcester, D. L., Abramson, J., Nanda, H., Rostovtseva, T. K. & Bezrukov, S. M. (2017). *Proc. Natl Acad. Sci. USA*, **114**, E3622–E3631.
- Jackman, A. J., Knoll, W. & Cho, N.-J. (2012). *Materials*, **5**, 2637–2657.
- Jagalski, V., Barker, R. D., Thygesen, M. B., Gotfryd, K., Krüger, M. B., Shi, L., Maric, S., Bovet, N., Moulin, M., Haertlein, M., Günther Pomorski, T., Loland, C. J. & Cárdenas, M. (2015). *Soft Matter*, **11**, 7707–7711.
- Jiang, Z., Heinrich, F., McGlinchey, R. P., Gruschus, J. M. & Lee, J. C. (2017). *J. Phys. Chem. Lett.* **8**, 29–34.
- Jo, S., Kim, T., Iyer, V. G. & Im, W. (2008). *J. Comput. Chem.* **29**, 1859–1865.
- Jorgensen, W. L., Chandrasekhar, J., Madura, J. D., Impey, R. W. & Klein, M. L. (1983). *J. Chem. Phys.* **79**, 926–935.
- Kienzle, P. A., Krycka, J., Patel, N. & Sahin, I. (2011). *Bumps* v.0.7.5.4. <https://github.com/bumps/bumps>.
- Knecht, S., Ricklin, D., Eberle, A. N. & Ernst, B. (2009). *J. Mol. Recognit.* **22**, 270–279.
- Kozuch, J., Weichbrodt, C., Millo, D., Giller, K., Becker, S., Hildebrandt, P. & Steinem, C. (2014). *Phys. Chem. Chem. Phys.* **16**, 9546–9555.
- Kučerka, N., Nieh, M.-P. & Katsaras, J. (2011). *Biochim. Biophys. Acta*, **1808**, 2761–2771.
- Kuhl, T. L., Leckband, D. E., Lasic, D. D. & Israelachvili, J. N. (1994). *Biophys. J.* **66**, 1479–1488.
- Lähdesmäki, K., Ollila, O. H. S., Koivuniemi, A., Kovanen, P. T. & Hyvönen, M. T. (2010). *Biochim. Biophys. Acta*, **1798**, 938–946.
- Lata, S., Reichel, A., Brock, R., Tampé, R. & Piehler, J. (2005). *J. Am. Chem. Soc.* **127**, 10205–10215.
- Lemasters, J. J., Bond, J. M., Chacon, E., Harper, I. S., Kaplan, S. H., Ohata, H., Trollinger, D. R., Herman, B. & Cascio, W. E. (1996). *EXS*, **76**, 99–114.
- Lemasters, J. J., Holmuhamedov, E. L., Czerny, C., Zhong, Z. & Maldonado, E. N. (2012). *Biochim. Biophys. Acta*, **1818**, 1536–1544.
- Maccarini, M., Gayet, L., Alcaraz, J. P., Liguori, L., Stidder, B., Watkins, E. B., Lenormand, J.-L. & Martin, D. K. (2017). *Langmuir*, **33**, 9988–9996.
- Majewski, J., Wong, J. Y., Park, C. K., Seitz, M., Israelachvili, J. N. & Smith, G. S. (1998). *Biophys. J.* **75**, 2363–2367.
- Maldonado, E. N. & Lemasters, J. J. (2014). *Mitochondrion*, **19**, 78–84.
- Mannella, C. A. (1998). *J. Struct. Biol.* **121**, 207–218.
- McGillivray, D. J., Valincius, G., Heinrich, F., Robertson, J. W., Vanderah, D. J., Febo-Ayala, W., Ignatjev, I., Lösche, M. & Kasianowicz, J. J. (2009). *Biophys. J.* **96**, 1547–1553.
- McGillivray, D. J., Valincius, G., Vanderah, D. J., Febo-Ayala, W., Woodward, J. T., Heinrich, F., Kasianowicz, J. J. & Lösche, M. (2007). *Biointerphases*, **2**, 21–33.
- Milner, S. T., Witten, T. A. & Cates, M. E. (1988). *Europhys. Lett.* **5**, 413–418.
- Mlayeh, L., Krammer, E.-M., Léonetti, M., Prévost, M. & Hombé, F. (2017). *Biochim. Biophys. Acta*, **1858**, 786–794.
- Mosior, M. & McLaughlin, S. (1992). *Biochim. Biophys. Acta*, **1105**, 185–187.
- Murphy, E. & Steenbergen, C. (2008). *Physiol. Rev.* **88**, 581–609.
- Nagle, J. F. & Tristram-Nagle, S. (2000). *Biochim. Biophys. Acta*, **1469**, 159–195.
- Nasr, M. L., Baptista, D., Strauss, M., Sun, Z.-Y. J., Grigoriu, S., Huser, S., Plückthun, A., Hagn, F., Walz, T., Hogle, J. M. & Wagner, G. (2017). *Nature Methods*, **14**, 49–52.
- Noskov, S. Y., Rostovtseva, T. K. & Bezrukov, S. M. (2013). *Biochemistry*, **52**, 9246–9256.
- Noskov, S. Y., Rostovtseva, T. K., Chamberlin, A. C., Teijido, O., Jiang, W. & Bezrukov, S. M. (2016). *Biochim. Biophys. Acta*, **1858**, 1778–1790.
- Noskov, S. Y. & Roux, B. (2008). *J. Mol. Biol.* **377**, 804–818.
- Nystrom, N. A., Levine, M. J., Roskies, R. Z. & Scott, J. R. (2015). *Proceedings of the 2015 XSEDE Conference: Scientific Advancements Enabled by Enhanced Cyberinfrastructure*, Article 30. St Louis: ACM.
- Olsson, M. H., Søndergaard, C. R., Rostkowski, M. & Jensen, J. H. (2011). *J. Chem. Theory Comput.* **7**, 525–537.
- Pastor, R. W. & MacKerell, A. D. (2011). *J. Phys. Chem. Lett.* **2**, 1526–1532.
- Radak, B. K., Chipot, C., Suh, D., Jo, S., Jiang, W., Phillips, J. C., Schulten, K. & Roux, B. (2017). *J. Chem. Theory Comput.* **13**, 5933–5944.
- Rappaport, S. M., Teijido, O., Hoogerheide, D. P., Rostovtseva, T. K., Berezhkovskii, A. M. & Bezrukov, S. M. (2015). *Eur. Biophys. J.* **44**, 465–472.
- Reina, S. & De Pinto, V. (2017). *Curr. Med. Chem.* **24**, 4447–4469.
- Robertson, J. W. F., Kasianowicz, J. J. & Banerjee, S. (2012). *Chem. Rev.* **112**, 6227–6249.
- Rostovtseva, T. K. & Bezrukov, S. M. (2008). *J. Bioenerg. Biomembr.* **40**, 163–170.
- Rostovtseva, T. K., Gurnev, P. A., Protchenko, O., Hoogerheide, D. P., Yap, T. L., Philpott, C. C., Lee, J. C. & Bezrukov, S. M. (2015). *J. Biol. Chem.* **290**, 18467–18477.
- Rostovtseva, T. K., Hoogerheide, D. P., Rovini, A. & Bezrukov, S. M. (2017). *Molecular Basis for Mitochondrial Signaling*, edited by T. K. Rostovtseva, pp. 185–215. Cham: Springer International.
- Rostovtseva, T. K., Sheldon, K. L., Hassanzadeh, E., Monge, C., Saks, V., Bezrukov, S. M. & Sackett, D. L. (2008). *Proc. Natl Acad. Sci. USA*, **105**, 18746–18751.
- Rostovtseva, T. K., Tan, W. & Colombini, M. (2005). *J. Bioenerg. Biomembr.* **37**, 129–142.
- Schneck, E., Schollier, A., Halperin, A., Moulin, M., Haertlein, M., Sferrazza, M. & Fragneto, G. (2013). *Langmuir*, **29**, 14178–14187.
- Shan, Y. B., Klepeis, J. L., Eastwood, M. P., Dror, R. O. & Shaw, D. E. (2005). *J. Chem. Phys.* **122**, 54101.
- Shannon, R. D. (1976). *Acta Cryst.* **A32**, 751–767.
- Shao, L., Kinnally, K. W. & Mannella, C. A. (1996). *Biophys. J.* **71**, 778–786.
- Shaw, D. E., Grossman, J., Bank, J. A., Batson, B., Butts, J. A., Chao, J. C., Deneroff, M. M., Dror, R. O., Even, A., Fenton, C. H., Forte, A., Gagliardo, J., Gill, G., Greskamp, B., Ho, C. R., Ierardi, D. J., Iserovich, L., Kuskin, J. S., Larson, R. H., Layman, T., Lee, L.-S., Lerer, A. K., Li, C., Killebrew, D., Mackenzie, K. M., Mok, S. Y.-H., Moraes, M. A., Mueller, R., Nociolo, L. J., Peticolas, J. L., Quan, T., Ramot, D., Salmon, J. K., Scarpazza, D. P., Schafer, U. B., Siddique, N., Snyder, C. W., Spengler, J., Tang, P. T. P., Theobald, M., Toma, H., Towles, B., Vitale, B., Wang, S. C. & Young, C. (2014). *Proceedings of the International Conference for High Performance Computing, Networking, Storage and Analysis*, pp. 41–53. Piscataway: IEEE.
- Shekhar, P., Nanda, H., Lösche, M. & Heinrich, F. (2011). *J. Appl. Phys.* **110**, 102216.
- Shoshan-Barmatz, V., De Pinto, V., Zweckstetter, M., Raviv, Z., Keinan, N. & Arbel, N. (2010). *Mol. Aspects Med.* **31**, 227–285.
- Shoshan-Barmatz, V., Krelm, Y. & Chen, Q. (2017). *Curr. Med. Chem.* **24**, 4435–4446.
- Song, J., Midson, C., Blachly Dyson, E., Forte, M. & Colombini, M. (1998). *Biophys. J.* **74**, 2926–2944.
- Soranzo, T., Martín, D. K., Lenormand, J.-L. & Watkins, E. B. (2017). *Sci. Rep.* **7**, 3399.
- Sumino, A., Uchihashi, T. & Oiki, S. (2017). *J. Phys. Chem. Lett.* **8**, 785–793.
- Teijido, O., Rappaport, S. M., Chamberlin, A., Noskov, S. Y., Aguilera, V. M., Rostovtseva, T. K. & Bezrukov, S. M. (2014). *J. Biol. Chem.* **289**, 23670–23682.
- Teijido, O., Ujwal, R., Hillerdal, C. O., Kullman, L., Rostovtseva, T. K. & Abramson, J. (2012). *J. Biol. Chem.* **287**, 11437–11445.

- Thiyagarajan, P. & Tiede, D. M. (1994). *J. Phys. Chem.* **98**, 10343–10351.
- Timmins, P. A., Leonhard, M., Weltzien, H. U., Wacker, T. & Welte, W. (1988). *FEBS Lett.* **238**, 361–368.
- Towns, J., Cockerill, T., Dahan, M., Foster, I., Gaither, K., Grimshaw, A., Hazlewood, V., Lathrop, S., Lifka, D., Peterson, G. D., Roskies, R., Scott, J. R. & Wilkens-Diehr, N. (2014). *Comput. Sci. Eng.* **16**, 62–74.
- Ujwal, R., Cascio, D., Colletier, J.-P., Faham, S., Zhang, J., Toro, L., Ping, P. & Abramson, J. (2008). *Proc. Natl Acad. Sci. USA*, **105**, 17742–17747.
- Vaish, A., Silin, V., Walker, M. L., Steffens, K. L., Krueger, S., Yeliseev, A. A., Gawrisch, K. & Vanderah, D. J. (2013). *Chem. Commun.* **49**, 2685–2687.
- Valincius, G., Meškauskas, T. & Ivanauskas, F. (2012). *Langmuir*, **28**, 977–990.
- Veneziano, R., Rossi, C., Chenal, A., Brenner, C., Ladant, D. & Chopineau, J. (2017). *Biointerphases*, **12**, 04E301.
- Villinger, S., Briones, R., Giller, K., Zachariae, U., Lange, A., de Groot, B. L., Griesinger, C., Becker, S. & Zweckstetter, M. (2010). *Proc. Natl Acad. Sci. USA*, **107**, 22546–22551.
- Vrugt, J. A., ter Braak, C. J. F., Diks, C. G. H., Robinson, B. A., Hyman, J. M. & Higdon, D. (2009). *Int. J. Nonlin. Sci. Numer. Simul.* **10**, 273–290.
- Wagner, M. L. & Tamm, L. K. (2000). *Biophys. J.* **79**, 1400–1414.
- Wetzer, B., Pum, D. & Sleytr, U. B. (1997). *J. Struct. Biol.* **119**, 123–128.
- Yeagle, P. L. (2014). *Biochim. Biophys. Acta*, **1838**, 1548–1559.
- Yildirim, M. A., Goh, K.-I., Cusick, M. E., Barabási, A.-L. & Vidal, M. (2007). *Nature Biotechnol.* **25**, 1119–1126.
- Zimmerberg, J. & Parsegian, V. A. (1986). *Nature (London)*, **323**, 36–39.